The Journal of Chemical Physics

RESEARCH ARTICLE | DECEMBER 11 2025

Quantum hierarchical Fokker–Planck equations with U(1) gauge fields [U(1)-QHFPE]: A computational framework for Aharonov–Bohm effects

Shoki Koyanagi ; Hyeonseok Yang ; Yoshitaka Tanimura

J. Chem. Phys. 163, 222502 (2025)
https://doi.org/10.1063/5.0302697

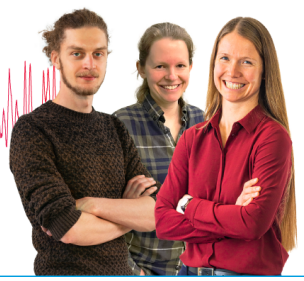

The Journal of Chemical Physics SOFTWARE pubs.aip.org/aip/jcp

Quantum hierarchical Fokker–Planck equations with U(1) gauge fields [U(1)-QHFPE]: A computational framework for Aharonov–Bohm effects

Cite as: J. Chem. Phys. 163, 222502 (2025); doi: 10.1063/5.0302697
Submitted: 16 September 2025 • Accepted: 12 November 2025 •
Published Online: 11 December 2025

Shoki Koyanagi,[a] Hyeonseok Yang, and Yoshitaka Tanimura

AFFILIATIONS

Department of Chemistry, Graduate School of Science, Kyoto University, Kyoto 606-8502, Japan

Note: This paper is part of the Special Topic, Yijing Yan Festschrift.
[a]**Author to whom correspondence should be addressed:** koyanagi.shoki.e00@kyoto-u.jp

ABSTRACT

We present a software package that solves the quantum Fokker–Planck equation with gauge fields, formulated within the hierarchical equations of motion framework [U(1)-QHFPE]. The framework rigorously preserves gauge invariance and rotational symmetry under non-Markovian and non-perturbative system–bath (S–B) interactions, enabling accurate simulations of transport phenomena such as the Aharonov–Bohm effect under thermal environments. In a strong S–B coupling regime, quantum S–B entanglement emerges naturally. The demonstration programs perform calculations of response functions in Aharonov–Bohm ring geometries with a mechanical potential that may induce quantum tunneling, thereby illustrating the software's capability to resolve topological quantum interference in dissipative open systems. Written in C++, the code includes a central processing unit version with highly readable OpenMP directives and a graphics processing unit version tailored for high-performance computing.

I. INTRODUCTION

Gauge invariance plays a foundational role in modern theoretical physics, serving as a guiding principle that determines the structure of physical laws.[1,2] By requiring that observable quantities remain invariant under local transformations of the underlying fields, gauge invariance ensures that only observables, such as electric and magnetic fields, appear in the theory, filtering out unphysical degrees of freedom. According to Noether's theorem, gauge symmetries are directly linked to conservation laws; for instance, U(1) symmetry implies charge conservation and naturally gives rise to interaction fields, with the photon emerging as the gauge boson of the U(1) group. Moreover, gauge invariance underlies the coherence of quantum phenomena, as exemplified by the Aharonov–Bohm (AB) effect,[3–5] where nonlocal phase shifts manifest in measurable interference patterns.

While the fundamental aspects of gauge-induced quantum effects have been extensively studied across various platforms, the influence of dissipation and thermal fluctuations, particularly those mediated by phonons, on quantum coherence remains incompletely understood.[6] In metallic and semiconductor nanorings, gate-induced resistance is often dominant, whereas in molecular nanorings, intrinsic resistance within the conductor becomes more relevant.[7–11] Although AB rings have been investigated through diverse configurations, including multi-ring networks,[12] embedded quantum dots,[13–19] multiterminal geometries,[20] and tunneling junctions,[21] the role of dissipation in these systems remains elusive.

Phonon-based models have been employed to analyze AB rings,[22,23] but they offer limited insight into gauge invariance, as they do not inherently encode the topological structure of electromagnetic potentials. Geometric features can be described using coordinate-based models such as the Caldeira–Leggett (CL) framework,[24–28] yet when applied to systems with rotational symmetry, such as quantum rotors and AB rings, these models fail to preserve entanglement under rotation due to the

symmetry-breaking nature of the thermal bath, yielding only semiclassical behavior.[29,30]

In our previous study,[31] we demonstrated that the introduction of a rotationally invariant system–bath (RISB) model is crucial for preserving quantum entanglement in rotating systems coupled to a thermal environment.[32–34] Building on this foundation, we developed a gauge-invariant formalism based on the HEOM, referred to as U(1)-HEOM, and its Fokker–Planck variant, U(1)-QHFPE, which is applicable to strongly coupled, non-Markovian open quantum systems. While the three-dimensional (3D) U(1)-HEOM formulation is computationally intensive, its reduction to two-dimensional (2D) geometries, such as AB rings, via U(1)-QHFPE yields substantial simplification. The present study extends our previous implementation, enhancing its generality and releasing the software as a publicly accessible tool for the broader research community.

Recent interest in quantum systems sensitive to gauge fields has grown rapidly,[35–38] particularly in cavity-quantum electrodynamics (cavity-QED) platforms, where quantum optical master equations are often employed under Markovian and factorized assumptions.[39,40] In contrast, the U(1)-QHFPE framework developed here enables the study of such systems under realistic conditions, capturing thermal excitation and dissipation effects at ultralow temperatures where quantum coherence is essential. As part of this study, we extend previous results by incorporating symmetric and antisymmetric correlation functions in non-Markovian and non-perturbative domains and further explore AB phase oscillations.

The remainder of this paper is organized as follows. Section II presents the theoretical models and derivation of the U(1)-QHFPE. Section III explains the details of the software. Section IV demonstrates the calculated results of response functions for the AB ring. Section V provides concluding remarks.

II. HIERARCHICAL EQUATIONS OF MOTION FOR AB RING SYSTEM

The AB system is modeled using the 2D RISB model expressed as $\hat{H}_{\rm tot}(t) = \hat{H}_A(t) + \hat{H}_{I+B}$ (see Fig. 1). Here, $\hat{H}_A(t)$ is the Hamiltonian of the AB system defined as

$$\hat{H}_A(t) = \frac{1}{2I_S}(\hat{p}_\theta - qr_0A_\theta)^2 + U(\hat{\theta};t). \tag{1}$$

Here, $\hat{p}_\theta, q, r_0$, and A_θ are the 2D angular momentum operators of the particle, electric charge, radius of the ring, and the azimuthal component of the vector potential, and $I_S = m_S r_0^2$ is the moment of inertia of the particle. We assume that the vector potential is time-independent and constant in the θ direction. We also introduce the potential, $U(\hat{\theta};t)$, where $\hat{\theta}$ is the angular position operator. The system–bath (S–B) interaction plus bath Hamiltonian $\hat{H}_{\rm I+B}$ is expressed as

$$\hat{H}_{I+B} = \sum_{\alpha}^{x,y}\sum_k \left\{ \frac{(\hat{p}_k^\alpha)^2}{2m_k^\alpha} + \frac{m_k^\alpha(\omega_k^\alpha)^2}{2}\left(\hat{q}_k^\alpha - \frac{c_k^\alpha \hat{V}_\alpha}{m_k^\alpha(\omega_k^\alpha)^2}\right)^2 \right\}, \tag{2}$$

where $\hat{p}_j^\alpha, \hat{x}_j^\alpha, m_j^\alpha$, and ω_j^α are the momentum and position operators, mass, and angular frequency of the jth mode of the bath in the α direction. The coefficient c_j^α is the coupling constant between the system and the jth mode of the α-direction bath. We set the system operator, $\hat{V}_\alpha$, as $\hat{V}_x = r_0\cos\hat{\theta}$ and $\hat{V}_y = r_0\sin\hat{\theta}$. We include the counterterms that are introduced to maintain the translational symmetry of the system.[41] The harmonic bath in the α direction is characterized by the spectral distribution function (SDF), defined as $J^\alpha(\omega) = \sum_k [\hbar(c_k^\alpha)^2/2m_k^\alpha\omega_k^\alpha]\delta(\omega-\omega_k^\alpha)$, and the inverse temperature, $\beta \equiv 1/k_{\rm B}T$, where $k_{\rm B}$ is the Boltzmann constant.

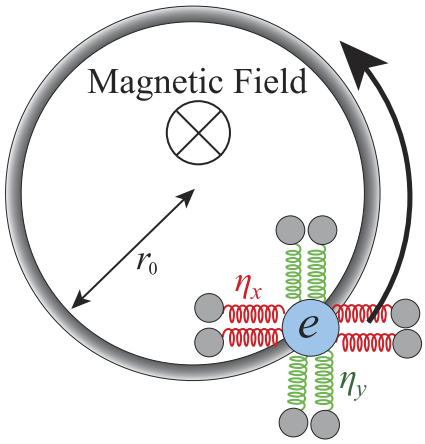

FIG. 1. Schematic illustration of the AB ring system in a dissipative environment. A charge (depicted as a blue circle) moves along a ring of fixed radius r_0 and is coupled to baths aligned along the x- and y-directions with coupling strengths η_x and η_y, respectively. A magnetic field confined within the ring generates a constant vector potential along the ring.

To easily adapt the HEOM formalism, we use the Drude SDF expressed as[42,43]

$$J^\alpha(\omega) = \frac{\hbar\eta_\alpha}{\pi}\frac{\gamma_\alpha^2\omega}{\gamma_\alpha^2+\omega^2}, \tag{3}$$

where γ_α and η_α are the inverse of the noise correlation time and S–B coupling strength in the $\alpha = x$ and y directions. It should be noted that $J^\alpha(\omega)$ does not have to be identical for different α. The HEOM is derived from the Feynman–Vernon influence functional, which traces out the bath degrees of freedom by leveraging their Gaussian statistics.[44] Within this framework, auxiliary density operators (ADOs) are employed to capture the non-Markovian memory inherent in S–B correlations.

To express the HEOM in phase space, we introduce a discretized Wigner transformation under periodic boundary conditions (DWT-PBC).[31,45] For the density operator in the 2D periodic system, this is defined as

$$W_{\{\boldsymbol{n}_\alpha\}}(p_n,\theta;t) = \frac{1}{2\pi\hbar}\int_{-L}^{L} e^{\frac{ip_n\varphi}{\hbar}}\rho_{\{\boldsymbol{n}_\alpha\}}\left(\theta-\frac{\varphi}{2},\theta+\frac{\varphi}{2};t\right)d\varphi, \tag{4}$$

where $\rho_{\{\boldsymbol{n}_\alpha\}}(\theta,\theta';t)$ and $W_{\{\boldsymbol{n}_\alpha\}}(p_n,\theta;t)$ are an ADO and an auxiliary Wigner distribution function (AWDF) in the HEOM formalism. The system period L is set to 2π, corresponding to the AB ring geometry. The subscript vectors $\{\boldsymbol{n}_\alpha\} = \{\boldsymbol{n}_x, \boldsymbol{n}_y\}$ are composed of non-negative integers, with each $\boldsymbol{n}_\alpha \equiv (n_\alpha^0, n_\alpha^1, \ldots, n_\alpha^{K_\alpha})$.

The function $W_{\{\boldsymbol{n}_\alpha\}}(p_n,\theta)$ is obtained for the periodic boundary condition. The momentum variable is discretized as $p_n = n\hbar/2$, where n is an integer. The AWDF is associated with the zero-index vectors, i.e., $\boldsymbol{n}_x = \mathbf{0}$ and $\boldsymbol{n}_y = \mathbf{0}$.

In the DWT-PBC representation, the U(1)-hierarchical quantum Fokker–Planck equations [U(1)-HQFPE] are expressed as[31]

$$\begin{aligned}\frac{\partial}{\partial t}W_{\{\boldsymbol{n}_\alpha\}}(p_n,\theta;t) = &-\left(\hat{\mathcal{L}}_{qm} + \sum_{\alpha}^{x,y}\sum_{j=0}^{K_\alpha} n_\alpha^j \nu_j^\alpha\right) W_{\{\boldsymbol{n}_\alpha\}}(p_n,\theta;t)\\ &+ \sum_{\alpha}^{x,y}\sum_{j=0}^{K_\alpha} \hat{\Phi}_\alpha W_{\{\boldsymbol{n}_\alpha+\boldsymbol{e}_\alpha^j\}}(p_n,\theta;t)\\ &+ \sum_{\alpha}^{x,y}\sum_{j=0}^{K_\alpha} n_\alpha^j \hat{\Theta}_j^\alpha W_{\{\boldsymbol{n}_\alpha-\boldsymbol{e}_\alpha^j\}}(p_n,\theta;t),\end{aligned} \tag{5}$$

where ν_j^α and K_α are the jth Padé frequency and the number of the Padé frequencies in the α direction.[46] The operator $\hat{\mathcal{L}}_{qm}$ is the quantum Liouvillian expressed as

$$\begin{aligned}-\hat{\mathcal{L}}_{qm}W(p_n,\theta) = &-\frac{p_n - qr_0A_\theta}{I_S}\frac{\partial W(p_n,\theta)}{\partial\theta} + \frac{r_0^2(\eta_y\gamma_y - \eta_x\gamma_x)}{4\hbar}\\ &\times \sin(2\theta)\left(W(p_{n+2},\theta) - W(p_{n-2},\theta)\right).\end{aligned} \tag{6}$$

Here, the second term on the right-hand side in Eq. (6) is the contribution from the counterterm and vanishes in the isotropic case. Systems involving a potential are presented in Appendix A. The other operators are defined as $\hat{\Phi}_\alpha = r_0 f_\alpha(\theta)\delta/\delta p_n \quad (\alpha = x, y)$,

$$\begin{aligned}\hat{\Theta}_0^\alpha W(p_n,\theta) = &\frac{\eta_\alpha r_0\gamma_\alpha}{\beta} f_\alpha(\theta)\left(1 + \sum_{k=1}^{K_\alpha}\frac{2\bar{\eta}_j^\alpha\gamma_\alpha^2}{\gamma_\alpha^2 - (\nu_j^\alpha)^2}\right)\frac{\delta W(p_n,\theta)}{\delta p_n}\\ &-\frac{\eta_\alpha r_0\gamma_\alpha^2}{2} g_\alpha(\theta)\left[W(p_{n+1},\theta) + W(p_{n-1},\theta)\right],\end{aligned} \tag{7}$$

and

$$\hat{\Theta}_j^\alpha = -f_\alpha(\theta)\frac{\eta_\alpha r_0\gamma_\alpha^2}{\beta}\frac{2\bar{\eta}_j^\alpha\nu_j^\alpha}{\gamma_\alpha^2 - (\nu_j^\alpha)^2}\frac{\delta}{\delta p_n} \quad (j = 1,\ldots,K_\alpha), \tag{8}$$

where $\bar{\eta}_j^\alpha$ is the jth Padé coefficient in the α direction.[46] The functions $f_\alpha(\theta)$ and $g_\alpha(\theta)$ are defined as $f_x(\theta) = -\sin\theta$, $f_y(\theta) = g_x(\theta) = \cos\theta$, and $g_y(\theta) = \sin\theta$, respectively. We also introduce the operator $\delta/\delta p_n$ defined as $\delta f(p_n)/\delta p_n \equiv [f(p_{n+1}) - f(p_{n-1})]/\hbar$, where $f(p_n)$ is an arbitrary function of p_n.

The U(1)-HQFPE formally includes an infinite set of AWDFs. To make the problem tractable, we introduce a truncation scheme at hierarchy depth $N_{\max}$, retaining only terms with $N \le N_{\max}$, where $N = \sum_\alpha^{x,y}\sum_{j=0}^{K_\alpha} n_\alpha^j$. Although a method for selecting $N_{\max}$ has been suggested in Ref. 47, it remains necessary to confirm the convergence of the dynamics with respect to this parameter.

III. SOFTWARE DETAILS

Written in C++, the software runs on Windows and Linux operating systems. It features parallel computation, a dynamically adjustable time step method, and an appropriate finite-difference method, each of which is elaborated upon in Secs. III A–III C.

A. Parallel processing

The software supports both CPU and GPU architectures. The U(1)-HQFPE [Eqs. (5)–(8)] defines a hierarchy of coupled differential equations, allowing each associated ADO to be propagated in parallel. In the GPU implementation, parallelization is further extended to the angular and momentum grid points. This structure enables efficient parallel computation. CPU execution employs OpenMP,[48–50] while GPU acceleration utilizes CUDA,[51–53] which requires a GPU produced by NVIDIA: GPU kernel speed improves when threads within a block share a uniform computational load. Accordingly, our software performs intra-block parallelization exclusively over the angular and momentum grid points in each ADO to maintain workload balance.

B. Adaptive time step size method

In our implementation, we adopt the Runge–Kutta–Fehlberg method,[54] which dynamically adjusts the time step size Δt to ensure that the numerical error remains below a user-defined tolerance parameter, TOL. Consequently, users are not required to manually specify an appropriate time step size. To estimate the local truncation error, we perform a single-step time evolution from t to $t + \Delta t$ using both fourth- and fifth-order integration formulas, denoted as $W_{\{\boldsymbol{n}\}}^{4\text{th}}(p_n,\theta;t+\Delta t)$ and $W_{\{\boldsymbol{n}\}}^{5\text{th}}(p_n,\theta;t+\Delta t)$, respectively.

Because evaluating the error across all AWDFs is computationally expensive, we estimate the error using only the system WDF at the point $\theta = 0$. The estimated error is defined as

$$\epsilon_{\text{err}} = \max_{p_n}\left|W_{\{\mathbf{0}\}}^{4th}(p_n,\theta=0;t+\Delta t) - W_{\{\mathbf{0}\}}^{5th}(p_n,\theta=0;t+\Delta t)\right|. \tag{9}$$

The error associated with a fourth-order integration method is of order $(\Delta t)^5$, indicating that the estimated error scales proportionally with the fifth power of the time step. Let ϵ_{err} denote the current error estimate, and Δt_{TOL} the time step that would yield an error equal to the prescribed tolerance TOL. Assuming a proportionality constant a, we have $a(\Delta t)^5 = \epsilon_{\text{err}}$ and $a(\Delta t_{\text{TOL}})^5 = \text{TOL}$. Solving these equations yields the time step adjustment formula

$$\Delta t_{\text{new}} = \left(C \times \text{TOL}/\epsilon_{\text{err}}\right)^{1/5}\Delta t, \tag{10}$$

where $C < 1$ is a safety factor introduced to prevent excessive error growth; in our implementation, we set $C = 0.99$. If $\epsilon_{\text{err}} > \text{TOL}$, the time evolution is retried using Δt_{new}. Otherwise, the simulation proceeds to the next time step with the updated value computed from Eq. (10).

C. Finite-difference method

To approximate the θ-derivative in the quantum Liouvillian, Eq. (6), we use a finite-difference method during time integration. The central scheme preserves energy but is numerically unstable, whereas the upwind scheme is stable but violates energy conservation. To reconcile these trade-offs, we adopt a velocity-adaptive hybrid scheme that ensures stability while retaining key physical properties. This scheme is expressed as follows:

$$\frac{\partial}{\partial\theta}f(\theta) \simeq \frac{\pm 1}{420\,\Delta\theta}[4f(\theta_{\pm 3}) - 42f(\theta_{\pm 2}) + 252f(\theta_{\pm 1}) + 105f(\theta_0) - 420f(\theta_{\mp 1}) + 126f(\theta_{\mp 2}) - 28f(\theta_{\mp 3}) + 3f(\theta_{\mp 4})], \tag{11}$$

where $\theta_n = \theta + n\,\Delta\theta$. We use the upper signs of $\pm$ and $\mp$ when $p_n - qr_0A_\theta \geq 0$, and the lower signs otherwise. Similar to the upwind scheme, this method adapts the direction of the finite difference according to the velocity. Like the central scheme, it incorporates both forward and backward components. This is a seventh-order method, with an error proportional to $(\Delta\theta)^7$.

IV. NUMERICAL DEMONSTRATION

A. Numerical details

To evaluate the numerical performance of our method, we consider an AB ring system with the following parameters: particle mass $m_S = 0.5$, ring radius $r_0 = 1.0$, elementary charge $q = -1.0$, and inverse noise correlation times $\gamma_x = \gamma_y = 1.0$. These settings yield a moment of inertia $I_S = 1.0$. Here, we set reduced Planck constant and Boltzmann constant to unity, setting $\hbar = 1$ and $k_B = 1$, respectively. The external potential is turned off, i.e., $U(\theta;\ t) = 0$. The eigenenergies of the system are then given by $E_n = (n - \tilde{\Phi})^2\hbar\omega_0$, where $n \in \mathbb{Z}$ and the characteristic rotational frequency are defined as $\omega_0 \equiv \hbar/(2I_S)$. Under the chosen parameters, we obtain $\omega_0 = 1.0$. We introduce the dimensionless magnetic flux $\tilde{\Phi} \equiv \Phi/\Phi_0$, where the enclosed magnetic flux is $\Phi \equiv A_\theta/(2\pi r_0)$. The flux quantum is defined as $\Phi_0 \equiv h/|q|$, representing the fundamental unit of magnetic flux quantization. For numerical calculations, we set the tolerance parameter as TOL $= 1.0 \times 10^{-10}$.

B. Equilibrium distribution

We begin by introducing the position distribution function (PDF), which is derived by integrating the system WDF over the momentum space. This procedure yields the spatial probability density along the angular coordinate θ and is formally defined as

$$P(\theta, t) = \frac{\hbar}{2}\sum_{n=-\infty}^{\infty} W_{\{\mathbf{0}\}}(p_n, \theta; t). \tag{12}$$

To illustrate the applicability of the developed code, we investigated a system coupled to an anisotropic bath. The S–B coupling strength in the x-direction was set to be twice that in the y-direction. We then considered three regimes: strong coupling ($\eta_x = 1.0$, $\eta_y = 0.5$), intermediate coupling ($\eta_x = 0.2$, $\eta_y = 0.1$), and weak coupling ($\eta_x = 0.02$, $\eta_y = 0.01$). The parameters η_x and η_y were chosen to ensure that the linear response spectra exhibit multiple rotational bands in the weak S–B coupling regime and a single overdamped peak in the strong coupling regime (see Fig. 3 in Ref. 31).

To perform the numerical integration of Eqs. (5)–(8), the number of Padé frequencies was set to $K_x = K_y = 2$ for the high-temperature case ($\beta = 1.0$) and $K_x = K_y = 4$ for the low-temperature case ($\beta = 2.5$). The truncation numbers were chosen as $N_{\max} = 7$, $N_{\max} = 6$, and $N_{\max} = 4$ for the strong, intermediate, and weak coupling regimes, respectively. The time evolution was carried out until the WDF of the system reached a steady state. The resulting WDF at that point was designated as the equilibrium distribution $W^{\mathrm{eq}}_{\{\mathbf{0}\}}(p_n, \theta)$.

Figure 2 presents the equilibrium PDF for strong (red curve), intermediate (green curve), and weak (blue curve) S–B coupling under isotropic conditions, shown for (a) the high-temperature case ($\beta = 1$) and (b) the low-temperature case ($\beta = 2.5$).

In Fig. 2(a), since the heat bath in the x-direction was coupled more strongly to the system than that in the y-direction, $P^{\mathrm{eq}}(\theta)$ exhibited maxima at $\theta = 0$ and π. This behavior reflected a purely quantum mechanical effect. In the classical limit, the distribution approached the uniform equilibrium form $\exp[-\beta\hat{H}_S]$, which is independent of θ, and no anisotropy was observed. Although the bath possessed 2D rotational symmetry, anisotropy emerged due to the fixed radial degree of freedom, which played a crucial role in the entanglement between the system and bath (bathentanglement).[43] At high temperature, the influence of discretized momentum was suppressed, and the position distribution showed negligible dependence on the magnetic field.

Figure 2(b) illustrates the low-temperature regime. The dashed curves correspond to the case with magnetic flux $\tilde{\Phi} = 0.5$. Compared to the high-temperature case, the amplitude was enhanced due to reduced decoherence from the bath, which weakened its disturbance of quantum entanglement. As the magnetic flux increased from 0 to 0.5, the oscillation amplitude grew, indicating stronger quantum interference effects. According to the Byers–Yang theorem,[55] physical observables in an AB ring, such as the oscillation amplitude and persistent current, exhibit periodicity in $\tilde{\Phi}$ with unit period. Consequently, the amplitude diminished in the flux interval $\tilde{\Phi} \in [0.5, 1]$.

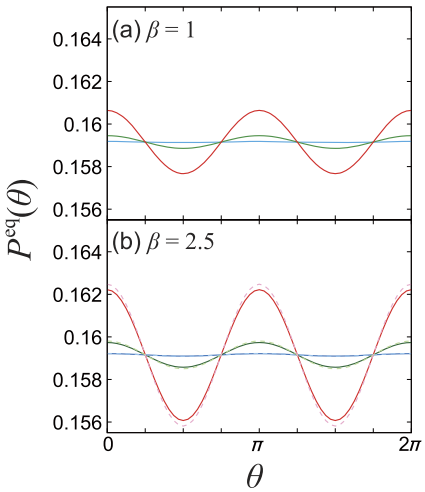

FIG. 2. Equilibrium PDFs were obtained for (a) the high-temperature case with $\beta = 1.0$ and (b) the low-temperature case with $\beta = 2.5$. The S–B coupling strength in the x-direction was set to be twice that in the y-direction. For each temperature, three regimes of anisotropic S–B coupling were considered: weak coupling (blue curves, $\eta_x = 0.02$, $\eta_y = 0.01$), intermediate coupling (green curves, $\eta_x = 0.2$, $\eta_y = 0.1$), and strong coupling (red curves, $\eta_x = 1.0$, $\eta_y = 0.5$). In panel (b), the influence of a magnetic flux $\tilde{\Phi} = 0.5$ is shown as dashed curves. At high temperature, however, the equilibrium distribution exhibits negligible dependence on the magnetic flux. Consequently, results for $\tilde{\Phi} = 0.5$ are omitted from panel (a).

The attenuation of anisotropic entanglement serves as strong evidence supporting the existence of quantum S–B entanglement.

C. Linear response function

In Fig. 3, we present the linear response (rotational) spectrum, defined as

$$\sigma(\omega) = \mathrm{Im}\left\{\int_0^\infty dt\ e^{i\omega t} R^{(1)}(t)\right\}, \tag{13}$$

where the linear response function (LRF) of the dipole moment is defined as $R^{(1)}(t) = i\langle[\cos\hat{\theta}(t), \cos\hat{\theta}(0)]\rangle/\hbar$, where

$$R^{(1)}(t) = \frac{i}{\hbar}\mathrm{Tr}_{\mathrm{tot}}\left\{\cos\hat{\theta}\hat{\mathcal{G}}(t)[\cos\hat{\theta}, \hat{\rho}_{\mathrm{tot}}^{\mathrm{eq}}]\right\}, \tag{14}$$

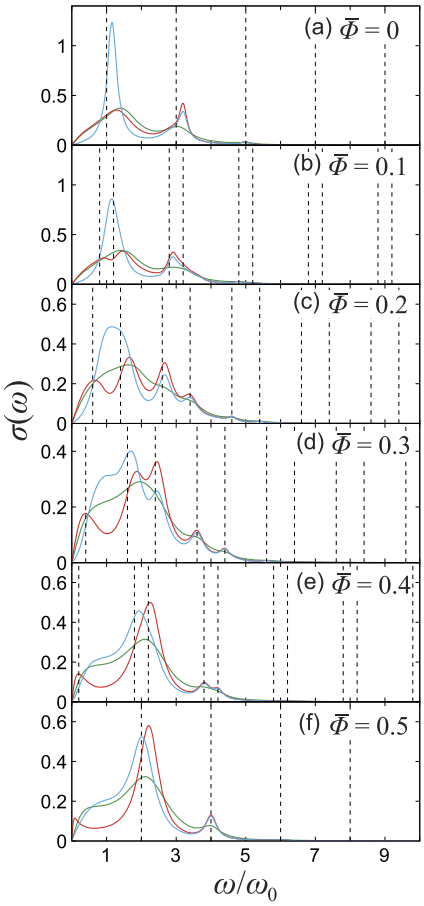

FIG. 3. Linear response spectra of the dipole moment for the AB ring, calculated under both isotropic and anisotropic environments. The S–B coupling strengths were set as follows: (red) $\eta_x = 1.0$, $\eta_y = 0.1$; (green) $\eta_x = 1.0$, $\eta_y = 1.0$; (blue) $\eta_x = 0.1$, $\eta_y = 1.0$. The magnetic flux values for each panel are (a) $\bar{\Phi} = 0.0$, (b) $\bar{\Phi} = 0.1$, (c) $\bar{\Phi} = 0.2$, (d) $\bar{\Phi} = 0.3$, (e) $\bar{\Phi} = 0.4$, and (f) $\bar{\Phi} = 0.5$. The black dashed line marks the peak position predicted by the system Hamiltonian without the baths.

and $\hat{\mathcal{G}}(t)$ is the time evolution operator for the total system in the absence of a laser interaction, and $\hat{\rho}_{\mathrm{tot}}^{\mathrm{eq}}$ is the equilibrium density operator for the total system.

The LRF can be computed in the Wigner representation through the following procedure: (1) apply the operator $\sin\theta\ (\delta/\delta p_n)$ to all AWDFs in the equilibrium state; (2) propagate the system under Eq. (5) from time $t = 0$ to t; (3) evaluate the LRF at time t as the expectation value of $\cos\hat{\theta}$, defined by

$$\langle\cos\hat{\theta}\rangle \equiv \frac{\hbar}{2}\sum_{n=-\infty}^{\infty}\int_0^{2\pi}\cos\theta\ W_{\{\mathbf{0}\}}(p_n, \theta; t)d\theta. \tag{15}$$

We set the inverse temperature to $\beta = 1.0$ and the S–B coupling strength parameters as follows: (red) $\eta_x = 1.0$, $\eta_y = 0.1$; (green) $\eta_x = 1.0$, $\eta_y = 1.0$; and (blue) $\eta_x = 0.1$, $\eta_y = 1.0$. These parameter sets were applied to panels (a)–(f), each corresponding to a different magnetic flux, $\bar{\Phi}$: (a) 0, (b) 0.1, (c) 0.2, (d) 0.3, (e) 0.4, and (f) 0.5.

Transitions induced by the external pulse were restricted to those between adjacent eigenstates of the system Hamiltonian, i.e., from the nth to the $n \pm 1$th states. The peak positions in the absence of baths were estimated by evaluating the energy differences $|E_n - E_{n\pm1}|$ for $n \in \mathbb{Z}$, leading to the analytical expression $\omega/\omega_0 = 2n + 1 \pm 2\bar{\Phi}$. These predicted positions were indicated by black dashed lines in Fig. 3.

As $\bar{\Phi}$ increased, the peaks in the red curves merged and became progressively sharper [Figs. 3(d)–3(f)]. This sharpening was a consequence of the enhanced ground-state particle velocity, resulting from the momentum shift induced by the vector potential. Accordingly, the particle shown in Figs. 3(e) and 3(f) coupled less effectively to the bath along the x-direction, leading to more pronounced spectral sharpening compared to the zero-field case. Notably, the peak in the low-frequency region deviated from the dashed line due to the influence of S–B entanglement.[29,30]

In contrast, under the blue curve configuration, the particle needed to migrate toward $\theta = 0$ and π in order to interact effectively with the bath along the y-direction. The peaks in the blue curves broadened with increasing magnetic field strength. This broadening arose from the enhanced coupling between the particle and the x-direction bath, facilitated by the momentum shift induced by the vector potential.

At higher frequencies, however, the red and blue curves converge. This convergence arises because the spectral contributions in the high-frequency domain originate from high-momentum states, where the particle motion is sufficiently rapid. Under such conditions, the anisotropic nature of the bath coupling is effectively averaged out, resulting in similar spectral profiles irrespective of the directional coupling configuration.

We also discuss the Markovian limit case in Appendix B, which was obtained by taking the high-temperature and Ohmic limits.

V. CONCLUSION

This paper enabled numerically "exact" dynamic simulations[43] of AB rings under non-Markovian and non-perturbative thermal environments, from low temperatures—where quantum effects become significant—to high-temperature limits corresponding to

the classical regime. In addition, it accounted for anisotropic environmental effects, as demonstrated by the examples presented in this paper.

The Wigner description was optimal for device simulations because it not only incorporated environmental effects to satisfy fluctuation and dissipation conditions but also facilitated geometric characterization and allowed for the addition of periodic or inflow/outflow boundaries.[56]

While this study focuses on isolated ring systems, verifying phase oscillations arising from the AB effect requires attaching leads to allow current flow. Such an extension is feasible through the generalization of the discrete Wigner transformation, which remains a subject for future investigation.

Furthermore, the proposed method is not limited to 1D systems; it is also applicable to electrons propagating in 2D or 3D geometries. This generality enables investigations into how dissipation and thermal effects affect geometrical phenomena such as the quantum Hall effect.

The Wigner representation facilitates the incorporation of time-dependent external fields of arbitrary strength and finds applications in quantum ratchet systems.[57] It further accommodates arbitrary potential profiles, including those relevant to resonant tunneling systems.[58] Moreover, this framework can be extended to systems with multiple potential energy surfaces,[59] thereby allowing for the inclusion of gauge fields in Berry phase analyses.[60]

The program is highly optimized and can run efficiently on personal computers. By promoting larger-scale parallelization and advanced GPU utilization, simulations such as those described earlier will become possible.

The fundamental principle of the U(1)-HEOM in gauge and rotational invariance lies in constructing the total Hamiltonian, including the thermal bath, in a manner that strictly preserves each symmetry. Therefore, equivalent results are expected from the pseudomode (PM) approach.[61–65] The present source code may serve as a reference when developing such programs. While simulating more realistic scenarios requires more computational resources than current classical hardware can provide, quantum computers may ultimately be required to perform such calculations.[66–68]

Such extensions should be pursued as necessary, in step with ongoing advances in computational technology and algorithmic development.

SUPPLEMENTARY MATERIAL

The numerical integration code for the U(1) quantum hierarchical Fokker–Planck equations, together with two demonstration codes for computing the equilibrium distribution and the linear response function, is provided in the supplementary material. The user manual is available in the `ReadMe.pdf` file.

ACKNOWLEDGMENTS

S.K. was supported by a Grant-in-Aid for JSPS Fellows (Grant No. 24KJ1373). Y.T. was supported by JST (Grant No. CREST 1002405000170). H.Y. acknowledges a fellowship supported by JST SPRING, the establishment of university fellowships toward the creation of science technology innovation (Grant No. JPMJSP2110).

AUTHOR DECLARATIONS

Conflict of Interest

The authors have no conflicts to disclose.

Author Contributions

Shoki Koyanagi: Data curation (equal); Software (equal); Writing – original draft (equal). **Hyeonseok Yang**: Formal analysis (supporting); Investigation (supporting). **Yoshitaka Tanimura**: Conceptualization (equal); Funding acquisition (equal); Supervision (equal).

DATA AVAILABILITY

The data that support the findings of this study are available from the corresponding author upon reasonable request.

APPENDIX A: SIMULATION INCLUDING MECHANICAL POTENTIAL

When a time-independent potential $U(\theta)$ is present, the quantum Liouvillian in Eq. (6) requires the following additional term:[31]

$$-\frac{1}{\hbar}\sum_{k=1}^{\infty}\left[u_k^{(c)}\sin(k\theta)-u_k^{(s)}\cos(k\theta)\right]\{W(p_{n+k},\theta)-W(p_{n-k},\theta)\}, \tag{A1}$$

where the potential is expressed in terms of its Fourier expansion as

$$U(\theta)=\sum_{k=1}^{\infty}\left[u_k^{(c)}\cos(k\theta)+u_k^{(s)}\sin(k\theta)\right]. \tag{A2}$$

Our software is capable of simulating dynamics under such potentials. In Fig. 4, we present the linear response functions for the potential $U(\theta)=-\cos\theta$ in the isotropic case, with parameters

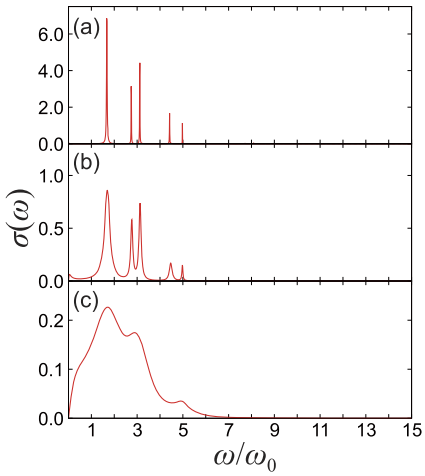

FIG. 4. Linear response spectra with the mechanical potential $U(\theta)=-\cos\theta$ are presented for the isotropic environment, $\eta_x=\eta_y\equiv\eta$ and $\gamma_x=\gamma_y=1$. The S-B coupling strength is set as follows for each figure: (a) $\eta=0.01$ (weak), (b) $\eta=0.1$ (intermediate), and (c) $\eta=1$ (strong).

set to $\eta_x = \eta_y \equiv \eta$ and $\gamma_x = \gamma_y = 1$. We use $\beta = 1$, $m_S = 0.5$, and $r_0 = 1$. The S-B coupling strength for each panel is as follows: (a) $\eta = 0.01$ (weak), (b) $\eta = 0.1$ (intermediate), and (c) $\eta = 1$ (strong). The spectral peaks are split due to the lifting of degeneracy induced by the potential.

APPENDIX B: MARKOVIAN LIMIT AND MASTER EQUATION

In the isotropic and high-temperature Ohmic case—corresponding to the zero noise correlation time limit $\gamma_x, \gamma_y \to \infty$ taken after the high-temperature limit in the Drude spectral density framework—we obtain the U(1)-QFPE expressed as[32]

$$\frac{\partial W(p_n,\theta)}{\partial t} = -\mathcal{L}_{qm} W(p_n,\theta) + \frac{\eta r_0^2}{\beta' \hbar^2}\left[W(p_{n+2},\theta) - 2W(p_n,\theta) + W(p_{n-2},\theta)\right] + \frac{\eta}{2m_S\hbar}\left[(p_{n+2} - qr_0A_\theta)W(p_{n+2},\theta) - (p_{n-2} - qr_0A_\theta)W(p_{n-2},\theta)\right], \tag{B1}$$

where $\beta' = \beta/\left(1 - \beta\hbar^2/(4I_S)\right)$ is the effective temperature that arises due to the constraint of a fixed radius. Note that the effective temperature in equation (QFPE) differs from that derived in the QHFPE formulation presented in our previous study.[31] In that derivation, the radial degree of freedom was explicitly included and subsequently reduced, whereas in the present formulation, the radius is fixed from the outset.

In Fig. 5, we examine the high-temperature case ($\beta = 0.2$) and present the results of the U(1)-QFPE without a magnetic field ($A_\theta = 0$) for weak (a, $\eta = 0.01$), intermediate (b, $\eta = 0.1$), and strong (c, $\eta = 1$) S-B coupling strengths. The red and blue curves show the results obtained from the U(1)-QFPE in Eq. (B1) and from Ref. 31, respectively. The black dashed curves represent the results from the U(1)-HQFPE in Eq. (5), evaluated with a very short noise correlation time ($\gamma_x = \gamma_y = 1000$). The red and black dashed curves show good agreement, whereas the blue curves deviate from the red ones. This confirms that the U(1)-HQFPE in Eq. (5) corresponds to the fixed-radius formulation.

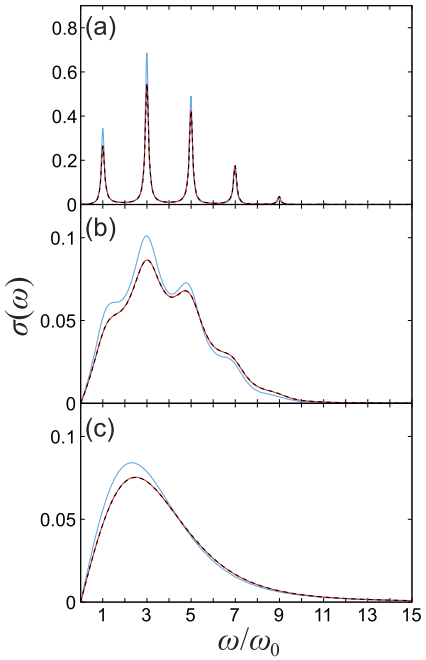

FIG. 5. Linear response spectra at a high temperature of $\beta = 0.2$ are presented for weak (a, $\eta = 0.01$), intermediate (b, $\eta = 0.1$), and strong (c, $\eta = 1$) S-B coupling strengths. The red and blue curves represent the results obtained from the U(1)-QFPE in Eq. (B1) and from Ref. 31, respectively. The black dashed curves correspond to the results of the U(1)-QHFPE with $\gamma_x = \gamma_y = 1000$. The blue curves were reproduced from Yang *et al.*, J. Chem. Phys. **163**, 144107 (2025), with the permission of AIP Publishing LLC.

REFERENCES

[1] S. Weinberg, *The Quantum Theory of Fields, Volume I: Foundations* (Cambridge University Press, Cambridge, 1995).
[2] S. Coleman, in *Lectures on Quantum Field Theory*, edited by B. G. ge Chen, D. E. Kaplan and A. E. Nelson (World Scientific Publishing Company, Singapore, 2019).
[3] Y. Aharonov and D. Bohm, "Significance of electromagnetic potentials in the quantum theory," Phys. Rev. **115**, 485–491 (1959).
[4] A. Tonomura, N. Osakabe, T. Matsuda, T. Kawasaki, J. Endo, S. Yano, and H. Yamada, "Evidence for Aharonov–Bohm effect with magnetic field completely shielded from electron wave," Phys. Rev. Lett. **56**, 792–795 (1986).
[5] A. Tonomura and F. Nori, "Disturbance without the force," Nature **452**, 298–299 (2008).
[6] X. Lu, J.-S. Wang, W. G. Morrel, X. Ni, C.-Q. Wu, and B. Li, "Thermoelectric effect in Aharonov–Bohm structures," J. Phys.: Condens. Matter **27**, 035301 (2014).
[7] A. Lahiri, K. Gharavi, J. Baugh, and B. Muralidharan, "Nonequilibrium Green's function study of magnetoconductance features and oscillations in clean and disordered nanowires," Phys. Rev. B **98**, 125417 (2018).
[8] T. Maaravi and O. Hod, "Simulating electron dynamics in open quantum systems under magnetic fields," J. Phys. Chem. C **124**, 8652–8662 (2020).
[9] A. Aharony, Y. Tokura, G. Z. Cohen, O. Entin-Wohlman, and S. Katsumoto, "Filtering and analyzing mobile qubit information via Rashba–Dresselhaus–Aharonov–Bohm interferometers," Phys. Rev. B **84**, 035323 (2011).
[10] M. W.-Y. Tu, W.-M. Zhang, J. Jin, O. Entin-Wohlman, and A. Aharony, "Transient quantum transport in double-dot Aharonov–Bohm interferometers," Phys. Rev. B **86**, 115453 (2012).
[11] B. Liu, Y. Li, J. Zhou, T. Nakayama, and B. Li, "Spin-dependent Seebeck effect in Aharonov–Bohm rings with Rashba and Dresselhaus spin–orbit interactions," Physica E **80**, 163–167 (2016).
[12] C. P. Umbach, C. Van Haesendonck, R. B. Laibowitz, S. Washburn, and R. A. Webb, "Direct observation of ensemble averaging of the Aharonov–Bohm effect in normal-metal loops," Phys. Rev. Lett. **56**, 386–389 (1986).
[13] A. Yacoby, M. Heiblum, D. Mahalu, and H. Shtrikman, "Coherence and phase sensitive measurements in a quantum dot," Phys. Rev. Lett. **74**, 4047–4050 (1995).
[14] A. L. Yeyati and M. Büttiker, "Aharonov–Bohm oscillations in a mesoscopic ring with a quantum dot," Phys. Rev. B **52**, R14360–R14363 (1995).
[15] K. Kobayashi, H. Aikawa, S. Katsumoto, and Y. Iye, "Tuning of the Fano effect through a quantum dot in an Aharonov–Bohm interferometer," Phys. Rev. Lett. **88**, 256806 (2002).
[16] S. Katsumoto, K. Kobayashi, H. Aikawa, A. Sano, and Y. Iye, "Quantum coherence in quantum dot—Aharonov–Bohm ring hybrid systems," Superlattices Microstruct. **34**, 151–157 (2003), part of Special Issue: Proceedings of the Joint 6th International Conference on New Phenomena in Mesoscopic Structures and 4th International Conference on Surfaces and Interfaces of Mesoscopic Devices.

[17]T. Nakanishi, K. Terakura, and T. Ando, "Theory of Fano effects in an Aharonov–Bohm ring with a quantum dot," Phys. Rev. B **69**, 115307 (2004).
[18]V. Moldoveanu, M. Ţolea, A. Aldea, and B. Tanatar, "Resonant and coherent transport through Aharonov–Bohm interferometers with coupled quantum dots," Phys. Rev. B **71**, 125338 (2005).
[19]R. Li, Y. Ding, Y. Yan, Y. Su, Y.-x. Huang, Z. Néda, E. O. Ayieta, G. Engelhardt, and J. Luo, "Waiting-time distribution as a sensitive probe of non-Markovian dephasing dynamics in a double-dot Aharonov–Bohm interferometer," Phys. Rev. B **111**, 035412 (2025).
[20]E. Strambini, V. Piazza, G. Biasiol, L. Sorba, and F. Beltram, "Impact of classical forces and decoherence in multiterminal Aharonov–Bohm networks," Phys. Rev. B **79**, 195443 (2009).
[21]Y. V. Nazarov, "Aharonov–Bohm effect in the system of two tunnel junctions," Phys. Rev. B **47**, 2768–2774 (1993).
[22]J. Jin, S. Wang, J. Zhou, W.-M. Zhang, and Y. Yan, "Manipulating quantum coherence of charge states in interacting double-dot Aharonov–Bohm interferometers," New J. Phys. **20**, 043043 (2018).
[23]G. Engelhardt and J. Cao, "Tuning the Aharonov–Bohm effect with dephasing in nonequilibrium transport," Phys. Rev. B **99**, 075436 (2019).
[24]A. O. Caldeira and A. J. Leggett, "Influence of dissipation on quantum tunneling in macroscopic systems," Phys. Rev. Lett. **46**, 211–214 (1981).
[25]A. O. Caldeira and A. J. Leggett, "Quantum tunnelling in a dissipative system," Ann. Phys. **149**, 374–456 (1983).
[26]A. J. Leggett, "Quantum tunneling in the presence of an arbitrary linear dissipation mechanism," Phys. Rev. B **30**, 1208–1218 (1984).
[27]Y.-C. Chen, "Macroscopic quantum tunneling in a dc SQUID," J. Low Temp. Phys. **65**, 133–147 (1986).
[28]A. J. Leggett, "Macroscopic quantum coherence and decoherence in SQUIDs," in *Macroscopic Quantum Coherence and Quantum Computing*, edited by D. V. Averin, B. Ruggiero, and P. Silvestrini (Springer, Boston, MA, 2001), pp. 1–6.
[29]Y. Suzuki and Y. Tanimura, "Two-time correlation function of a two-dimensional quantal rotator in a colored noise," J. Phys. Soc. Jpn. **71**, 2414–2426 (2002).
[30]Y. Suzuki and Y. Tanimura, "Two-dimensional spectroscopy for a two-dimensional rotator coupled to a Gaussian–Markovian noise bath," J. Chem. Phys. **119**, 1650–1660 (2003).
[31]H. Yang, S. Koyanagi, and Y. Tanimura, "Quantum hierarchical Fokker–Planck equations with U(1) gauge fields: Application to the Aharonov–Bohm ring," J. Chem. Phys. **163**, 144107 (2025).
[32]Y. Iwamoto and Y. Tanimura, "Linear absorption spectrum of a quantum two-dimensional rotator calculated using a rotationally invariant system-bath Hamiltonian," J. Chem. Phys. **149**, 084110 (2018).
[33]Y. Iwamoto and Y. Tanimura, "Open quantum dynamics of a three-dimensional rotor calculated using a rotationally invariant system-bath Hamiltonian: Linear and two-dimensional rotational spectra," J. Chem. Phys. **151**, 044105 (2019).
[34]L. Chen, M. F. Gelin, and W. Domcke, "Orientational relaxation of a quantum linear rotor in a dissipative environment: Simulations with the hierarchical equations-of-motion method," J. Chem. Phys. **151**, 034101 (2019).
[35]O. Di Stefano, A. Settineri, V. Macrì, L. Garziano, R. Stassi, S. Savasta, and F. Nori, "Resolution of gauge ambiguities in ultrastrong-coupling cavity quantum electrodynamics," Nat. Phys. **15**, 803–808 (2019).
[36]L. Garziano, A. Settineri, O. Di Stefano, S. Savasta, and F. Nori, "Gauge invariance of the Dicke and Hopfield models," Phys. Rev. A **102**, 023718 (2020).
[37]S. Savasta, O. Di Stefano, A. Settineri, D. Zueco, S. Hughes, and F. Nori, "Gauge principle and gauge invariance in two-level systems," Phys. Rev. A **103**, 053703 (2021).
[38]A. Settineri, O. Di Stefano, D. Zueco, S. Hughes, S. Savasta, and F. Nori, "Gauge freedom, quantum measurements, and time-dependent interactions in cavity QED," Phys. Rev. Res. **3**, 023079 (2021).
[39]W. Salmon, C. Gustin, A. Settineri, O. Di Stefano, D. Zueco, S. Savasta, F. Nori, and S. Hughes, "Gauge-independent emission spectra and quantum correlations in the ultrastrong coupling regime of open system cavity-QED," Nanophotonics **11**, 1573–1590 (2022).
[40]K. Akbari, W. Salmon, F. Nori, and S. Hughes, "Generalized Dicke model and gauge-invariant master equations for two atoms in ultrastrongly-coupled cavity quantum electrodynamics," Phys. Rev. Res. **5**, 033002 (2023).
[41]Y. Tanimura and P. G. Wolynes, "Quantum and classical Fokker–Planck equations for a Gaussian–Markovian noise bath," Phys. Rev. A **43**, 4131–4142 (1991).
[42]Y. Tanimura, "Stochastic Liouville, Langevin, Fokker–Planck, and master equation approaches to quantum dissipative systems," J. Phys. Soc. Jpn. **75**, 082001 (2006).
[43]Y. Tanimura, "Numerically 'exact' approach to open quantum dynamics: The hierarchical equations of motion (HEOM)," J. Chem. Phys. **153**, 020901 (2020).
[44]R. P. Feynman and F. L. Vernon, Jr., "The theory of a general quantum system interacting with a linear dissipative system," Ann. Phys. **24**, 118–173 (1963).
[45]J. P. Bizarro, "Weyl–Wigner formalism for rotation-angle and angular-momentum variables in quantum mechanics," Phys. Rev. A **49**, 3255 (1994).
[46]J. Hu, R.-X. Xu, and Y. Yan, "Communication: Padé spectrum decomposition of Fermi function and Bose function," J. Chem. Phys. **133**, 101106 (2010).
[47]A. Ishizaki and Y. Tanimura, "Quantum dynamics of system strongly coupled to low-temperature colored noise bath: Reduced hierarchy equations approach," J. Phys. Soc. Jpn. **74**, 3131–3134 (2005).
[48]J. Strümpfer and K. Schulten, "Open quantum dynamics calculations with the hierarchy equations of motion on parallel computers," J. Chem. Theory Comput. **8**, 2808–2816 (2012).
[49]Q. Shi, L. Chen, G. Nan *et al.*, "Efficient hierarchical Liouville space propagator to quantum dissipative dynamics," J. Chem. Phys. **130**, 084105 (2009).
[50]M. Noack, A. Reinefeld, T. Kramer, and T. Steinke, "DM-HEOM: A portable and scalable solver-framework for the hierarchical equations of motion," in *2018 IEEE International Parallel and Distributed Processing Symposium Workshops (IPDPSW)* (IEEE, 2018), pp. 947–956.
[51]C. Kreisbeck, T. Kramer, M. Rodríguez, and B. Hein, "High-performance solution of hierarchical equations of motion for studying energy transfer in light-harvesting complexes," J. Chem. Theory Comput. **7**, 2166–2174 (2011).
[52]M. Tsuchimoto and Y. Tanimura, "Spins dynamics in a dissipative environment: Hierarchal equations of motion approach using a graphics processing unit (GPU)," J. Chem. Theory Comput. **11**, 3859–3865 (2015).
[53]N. Lambert, E. Giguère, P. Menczel, B. Li, P. Hopf, G. Suárez, M. Gali, J. Lishman, R. Gadhvi, R. Agarwal *et al.*, "QuTip 5: The quantum toolbox in python," arXiv:2412.04705 (2024).
[54]E. Fehlberg, "Low-order classical Runge–Kutta formulas with stepsize control and their application to some heat transfer problems," NASA Technical Report No. 315, 1969.
[55]N. Byers and C. N. Yang, "Theoretical considerations concerning quantized magnetic flux in superconducting cylinders," Phys. Rev. Lett. **7**, 46–49 (1961).
[56]W. R. Frensley, "Boundary conditions for open quantum systems driven far from equilibrium," Rev. Mod. Phys. **62**, 745–791 (1990).
[57]A. Kato and Y. Tanimura, "Quantum suppression of ratchet rectification in a Brownian system driven by a biharmonic force," J. Phys. Chem. B **117**, 13132–13144 (2013); arXiv:1305.1402.
[58]A. Sakurai and Y. Tanimura, "Self-excited current oscillations in a resonant tunneling diode described by a model based on the Caldeira–Leggett Hamiltonian," New J. Phys. **16**, 015002 (2014).
[59]T. Ikeda and Y. Tanimura, "Probing photoisomerization processes by means of multi-dimensional electronic spectroscopy: The multi-state quantum hierarchical Fokker–Planck equation approach," J. Chem. Phys. **147**, 014102 (2017).
[60]T. Ikeda and Y. Tanimura, "Phase-space wavepacket dynamics of internal conversion via conical intersection: Multi-state quantum Fokker–Planck equation approach," Chem. Phys. **515**, 203–213 (2018).
[61]R. Martinazzo, B. Vacchini, K. H. Hughes, and I. Burghardt, "Communication: Universal Markovian reduction of Brownian particle dynamics," J. Chem. Phys. **134**, 011101 (2011).
[62]D. Tamascelli, A. Smirne, S. F. Huelga, and M. B. Plenio, "Nonperturbative treatment of non-Markovian dynamics of open quantum systems," Phys. Rev. Lett. **120**, 030402 (2018).

[63]N. Lambert, S. Ahmed, M. Cirio, and F. Nori, "Modelling the ultra-strongly coupled spin-boson model with unphysical modes," Nat. Commun. **10**, 3721 (2019).
[64]G. Pleasance, B. M. Garraway, and F. Petruccione, "Generalized theory of pseudomodes for exact descriptions of non-Markovian quantum processes," Phys. Rev. Res. **2**, 043058 (2020).
[65]P. Menczel, K. Funo, M. Cirio, N. Lambert, and F. Nori, "Non-Hermitian pseudomodes for strongly coupled open quantum systems: Unravelings, correlations, and thermodynamics," Phys. Rev. Res. **6**, 033237 (2024).
[66]X. Dan, E. Geva, and V. S. Batista, "Simulating non-Markovian quantum dynamics on NISQ computers using the hierarchical equations of motion," J. Chem. Theory Comput. **21**, 1530–1546 (2025).
[67]N. Lambert, M. Cirio, J.-D. Lin, P. Menczel, P. Liang, and F. Nori, "Fixing detailed balance in ancilla-based dissipative state engineering," Phys. Rev. Res. **6**, 043229 (2024).
[68]Z. Shi, H. Zhou, L. Huang, R. Xie, and L. Wang, "Hierarchical equations of motion solved with the multiconfigurational Ehrenfest ansatz," J. Chem. Phys. **163**, 224103 (2025).